Battery Capacity Fading Estimation Using a Force-Based Incremental Capacity Analysis

Nassim A. Samad,[a,z] Youngki Kim,[b] Jason B. Siegel,[a,*] and Anna G. Stefanopoulou[a,*]

[a]*Department of Mechanical Engineering, University of Michigan, Ann Arbor, Michigan 48109, USA*
[b]*Ann Arbor Technical Center, Southwest Research Institute, Ann Arbor, Michigan 48105, USA*

Traditionally health monitoring techniques in lithium-ion batteries rely on voltage and current measurements. A novel method of using a mechanical rather than electrical signal in the incremental capacity analysis (ICA) method is introduced in this paper. This method derives the incremental capacity curves based on measured force (ICF) instead of voltage (ICV). The force is measured on the surface of a cell under compression in a fixture that replicates a battery pack assembly and preloading. The analysis is performed on data collected from cycling encased prismatic Lithium-ion Nickel-Manganese-Cobalt Oxide (NMC) cells. For the NMC chemistry, the ICF method can complement or replace the ICV method for the following reasons. The identified ICV peaks are centered around 40% of state of charge (SOC) while the peaks of the ICF method are centered around 70% of SOC indicating that the ICF can be used more often because it is more likely that an electric vehicle (EV) or a plug-in hybrid electric vehicle (PHEV) will traverse the 70% SOC range than the 40% SOC. In addition the Signal to Noise ratio (SNR) of the force signal is four times larger than the voltage signal using laboratory grade sensors. The proposed ICF method is shown to achieve 0.42% accuracy in capacity estimation during a low C-rate constant current discharge. Future work will investigate the application of the capacity estimation technique under charging and operation under high C-rates by addressing the transient behavior of force so that an online methodology for capacity estimation is developed.
 [DOI: 10.1149/2.0511608jes]

Manuscript submitted March 11, 2016; revised manuscript received May 16, 2016. Published May 27, 2016. This article is a version of Paper 450 from the San Diego, California, Meeting of the Society, May 29- June 2, 2016.

Lithium-ion (Li-ion) batteries have been one of the most popular choices for use as power sources in electric vehicles (EVs) and hybrid electric vehicles (HEVs). Their popularity stems from their high energy and power densities and their ability to achieve long driving ranges. However, their performance suffers from aging and degradation[1,29,33] that should be recognized and accounted for to achieve efficient long term performance. Thus significant research has been focused on trying to understand the aging mechanisms in Li-ion cells and connect them with measurable and identifiable features in an effort to improve the utilization and reliability of these cells through the battery management system (BMS). The power capability and capacity are both important factors used to determine the state of health (SOH). The SOH of a battery is usually quantified using either resistance growth[3,8,17,18,25,32] or capacity loss.[9,13,35,36] This paper focuses on the capacity fading dimension of SOH.

Several methods haven been introduced in literature for the evaluation of the aging in battery. Traditional and conventional methods rely on voltage measurements. In Cyclic Voltammetry (CV), the electrode potential is ramped linearly versus time.[12] And the resulting current is plotted vs voltage. Peaks in the CV indicate reactions and, a shift in their location is correlated with aging. The probability density function (PDF) method applies a histogram to the charge/discharge voltage data of a cell to extract the PDF curve.[10] As the cell degrades, the PDF curve shifts which allows for aging detection. Another widely known method is the Differential Voltage (DV) method.[5,14,34] The method plots the differential of voltage over capacity with respect to capacity (dV/dQ versus Q). Finally, one of the most recent methods in literature is the incremental capacity analysis (ICA).[7,14,35,36] In many cell chemistries, the cells are characterized by a voltage plateau for a wide range of SOCs. The ICA method plots the incremental capacity over voltage (dQ/dV) with respect to voltage, which allows for clearly identifiable peaks where their location with respect to voltage is correlate with capacity fading. This method has been recently shown to predict capacity fade with less than 1% error.[35]

Although the ICA method has been shown to be accurate in estimating capacity fade, it still has some major setbacks. First, the method is sensitive to noise and accuracy of voltage measurements. Computing the differential of voltage in areas with flat voltage vs SOC could result in noise (since $dV \approx 0$). This is especially the case in Lithium Iron Phosphate (LFP) cells which are characterized by flat voltage curves. Second, depending on the chemistry and anode/cathode matching, the ICA peaks in discharge are centered around the low SOC range. For example, in the case of a Nickel-Manganese-Cobalt Oxide (NMC) cell, the ICA peaks are centered around 40%. This means that the cell has to operate at the low SOC range (below 40%) in order to estimate and monitor capacity fading.

In more recent work, focus has been directed toward understanding and modeling the mechanical behavior of batteries[19,20,23,31] in an attempt to provide better means to estimate the states of a battery, mainly SOC and SOH. In Ref. 20, it has been shown that force measurements can decrease the mean and standard deviation of the SOC estimation error by up to 50% in some regions. The authors in Ref. 23 show that, unlike voltage which changes minimally with C-rate, strain can vary significantly and can be used for characterizing dynamic system states. More recently, other methods have investigated the first and second derivative of strain with respect to charge, by measuring the strain on the surface of the battery during charging and discharging. Note that these methods have been applied to a battery that is not constrained in any way and is allowed to expand freely. In Ref. 31, it is shown that the second derivative of strain with respect to capacity exhibits similar shift in peaks as those resulting from the DV method as the cell degrades in a more consistent and reliable manner. Also, in a battery pack where cell expansion is limited, measuring the strain can be hard and can result in low signal to noise ratios, which makes the methods, such as that presented in Ref. 31, difficult to implement.

This paper focuses on the mechanical behavior of packaged cells and how the measured force can be used for better capacity estimation. The ICA method is used to derive the IC curves from the measured force. In Li-ion batteries, charging causes volume change or swelling of the electrodes as the lithium ions intercalate in the negative electrode. The authors in Ref. 31 propose a method which uses the measurements of the battery free expansion. However, in applications where the batteries are constrained in a pack to prevent expansion, as in the case in a real vehicle application, the swelling causes a stress. This stress can be measured using a force sensor mounted on

*Electrochemical Society Member.
[z]E-mail: nassimab@umich.edu

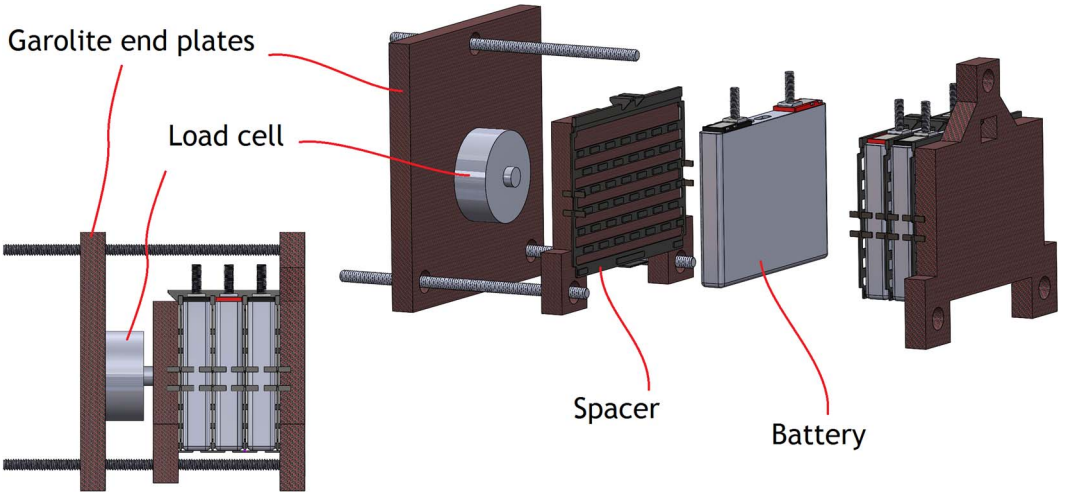

Figure 1. Schematic showing 3 lithium ion cells sandwiched between two garolite end plates. A load cell is installed for measuring the force due to cell expansion. The end plates are bolted together while the garolite middle plate is meant to act as a separator between the cells and the load cell.

the end plates of a cell pack or module as described in Sec. Force measurements. The resulting measured force can thus be used in the incremental capacity analysis.

Incremental capacity analysis based on force measurements (ICF) is promising technique since the percent change in force (68%) is much larger than voltage (27%), and the minimum slope in the force curve is 0.5% full scale / % SOC while for voltage it is 0.1% full scale / % SOC. The peak in force derivative, dF/dQ, is 62 lbs/Ah, while for voltage, dV/dQ, it is 0.2 V/Ah. The standard deviation in voltage measurement is around 1 mV yielding a SNR of 1.3, while for the force sensor it is 0.2 N (0.04 lbs) and the resulting SNR is 4. This makes the force derivative easier to compute and less sensitive to noise which permits the use of inexpensive force sensors. Since the relative change in force is larger than voltage, the resulting signal to noise ratio when deriving the incremental capacity curves is larger for the ICF than the ICV as shown in Sec. Incremental capacity analysis for bulk capacity estimation. In the case of an NMC cell, the ICF peaks occur around 70% SOC while those of the ICV occur around 40% SOC. Hence the proposed ICF based SOH monitoring could be updated more frequently within the regular use of an EV or PHEV involving short trips where the SOC does not usually fall below 50% .

This paper is organized as follows: first, Experimental section shows the experimental fixture for measuring force and the experimental protocol used to probe degradation. The measured capacity fade, calculated by a 1C discharge, are presented in Capacity. Then the ICF method is shown in Incremental capacity analysis for bulk capacity estimation and Incremental capacity analysis for individual cell capacity estimation for bulk and individual cell capacity estimation. Finally, the C-rate dependence of the ICF method is investigated in Sec. C-rate dependence.

Experimental

Force measurements.—The batteries used in this study are Lithium Nickel-Manganese-Cobalt (NMC) Oxide battery. Each battery is $120 \times 85 \times 12.7$ mm with a 5Ah nominal capacity. A flat-wound jelly roll is encased inside the aluminum hard shell of the battery. The jelly roll does not fill the whole enclosure and thus there are air gaps around the sides and the top of the cell. The structure of the jelly roll results in electrode expansion in the direction perpendicular to its largest face.[23] The NMC cells were extracted from a HEV battery pack. In a vehicle battery pack, multiple cells are stacked together in an array and constrained together under compression to prevent expansion. Thus, as these cells are cycled in the vehicle pack, it will be easier to measure stress and not strain. To emulate the typical pack conditions for identical fixtures were fabricated consisting of three Li-ion batteries each as shown in Figure 1. Since the estimation of SOH or capacity fading is the primary objective of this study, the four fixtures are intended to test the effect of nominal operating SOC and initial preloading conditions on the degradation rates of cells. The details about the degradation experiments are presented in Sec. Degradation experiments. Each fixture has two garolite end plates in between which are the 3 batteries, a garolite middle plate and a load cell. The fixture is clamped together using bolts with lock nuts to prevent it from loosening. The load cell is a 500 lbs (LC305-500) Omega load cell sensor (strain gauge type) with an accuracy of 1 lbs. The garolite middle plate is meant to act as a separator between the load cell and the battery cells. This is to prevent the load cell from acting directly on the battery and to uniformly distribute the force. The middle plate is also slightly lifted off the ground as to not allow the ground friction to absorb some of the force exerted by the cells. The cells are separated by a plastic spacer, also taken from the HEV pack, with dimples on it to allow for air to flow between the cells for cooling purposes and also maintain compression between the batteries.

Since thermal expansion of the cell material can result in measurable strain or expansion in the cells,[21] affecting the force, it is important that the temperature of the cells be measured, and the thermal expansion is taken into account. Resistance temperature detector (RTD) sensors were instrumented on the middle battery of each of fixture. The RTD arrays were made from flexible kapton substrate and composed of platinum with a nominal 100 Ω resistance. They are less than 100 μm thick and have a 0.5°C accuracy. These RTDs have been shown to improve the observability and convergence of the core temperature estimation of the battery as compared to a conventional thermistor sensor placed close to the tabs.[27] The accurate estimation of the cell core temperature is important at high C-rates for clarifying how much of the observed force is due to thermal expansion and how much is attributed to lithium ion intercalation. All data is sampled at a 1 Hz rate. The fixtures are placed in a thermal environmental chamber for ambient temperature control.

Degradation experiments.—Typically, quantitative analysis of degradation is either based on capacity fade[9,13] or growth in internal resistance of the battery.[3,8,17,18,25,32] In this paper, the focus is on capacity fade since it is very important for the range of EVs, and could be important in the future for hybrids if the operating SOC window for these batteries widens. Since aging related mechanisms are shown to be coupled to mechanical effects,[33,37] the 4 fixtures are designed to test degradation while cycling with the same current profile at different states of charge (SOC) and initial preloading conditions. Capacity fade is shown to be slower at lower SOCs as shown in other

Table I. Operating conditions for all 4 fixtures.

(1^{st} stage / 2^{nd} stage)	Fixture 1	Fixture 2	Fixture 3	Fixture 4
Initial SOC [%]	33/40	50/50	66/60	50/50
Ambient Temperature [°C]	10/25	10/25	10/25	10/25
Initial Preload [lbs]	168/168	168/168	168/168	334/334
ΔSOC [%]	20/26	20/26	20/26	20/26
ΔVoltage [V]	0.46/0.62	0.41/0.48	0.43/0.48	0.41/0.47
ΔForce [lbs]	47/81	33/66	21/47	37/71

studies,[11,16,28] perhaps due to the lower bulk stresses on the battery.[15] As such, Table I shows the nominal SOC and preloading force for all 4 fixtures. The nominal SOC is defined as the nominal SOC at which the cell is being cycled at, and preload is the initial force that is used to clamp the cells before any degradation experiments. The preload is set at an initial SOC of 50% at 25°C for all 4 fixtures.

Note that this is a two stage degradation experiment. During the first stage of the experiment, fixtures 1 through 4 are set to {33, 50, 66, 50}% initial SOCs and a preload of {168, 168, 168, 334} lbs respectively at the ambient temperature of 10°C. During the second stage of the experiment, the current is scaled by a factor of 1.3 and the ambient temperature is raised to 25°C. Since the current is scaled in the second stage, the initial SOCs for fixtures 1 and 3 had to be moved closer to 50% SOC, otherwise voltage limits would be violated due to the high current rates. Specifically, the fixtures 1 through 4 are set to {40, 50, 60, 50}% initial SOCs without changing the preload. The two stage experiment was designed to develop a predictive model for battery capacity loss considering operating conditions such as accumulated Ah-processed, operating SOC and temperature.[28] The elevated current and temperature of the 2^{nd} stage were chosen to investigate conditions that would result in faster degradation rates. The same cells were used as only a minor capacity loss was observed at the end of the first stage, as opposed to using fresh cells.

A charge sustaining current profile is used for cycling the cells. The battery current profile is the result of the vehicle hybrid power split captured during an actual drive. The fixtures are connected in series and hence the same current passed through all the cells in all fixtures. The details of the current profile is detailed in Appendix A. After cycling the cells continuously for 450 cycles, a test to measure capacity of the cells is performed. The corresponding procedure for measuring capacity is detailed in Appendix B. After the capacity test, the process was repeated. The entire testing involved 3500 cycles of stage 1 type experiments followed by 2700 cycles of stage 2 type experiments for a total of 64 kAh. This corresponds to 95000 total miles traveled for the HEV.

Results

In the following sections, the capacity fading results of the degradation experiments are shown in section Capacity fading. Sections Incremental capacity analysis for bulk capacity estimation and Incremental capacity analysis for individual cell capacity estimation present the results of using bulk force measurements for offline bulk fixture capacity estimation and individual cell capacity estimation respectively using incremental capacity analysis.

Capacity fading.—To study the capacity fading mechanisms in the different fixtures, an approximately 20 min charge sustaining current profile, which is detailed in Appendix A, is applied to the cells continuously for 450 cycles. After that a capacity test is applied to the cells using a 5 A (1 C-rate) discharge current. The protocol for the capacity test is detailed in Appendix B.

The results of the capacity fading are plotted in Fig. 2. The dashed vertical line represents the moment at which the second stage degradation experiment started. Since each fixture has 3 cells, the average capacity for each fixture is plotted against the number of cycles. The plot shows both absolute and percent capacity fade. Also, since each fixture is comprised of 3 cells each, a bar is used to represent the span of capacities of each of the 3 cells at each point. Notice, for example, that around 2700 cycles, the difference in capacity between the 3 cells in fixture 4 is around 2.5%. This is the largest imbalance

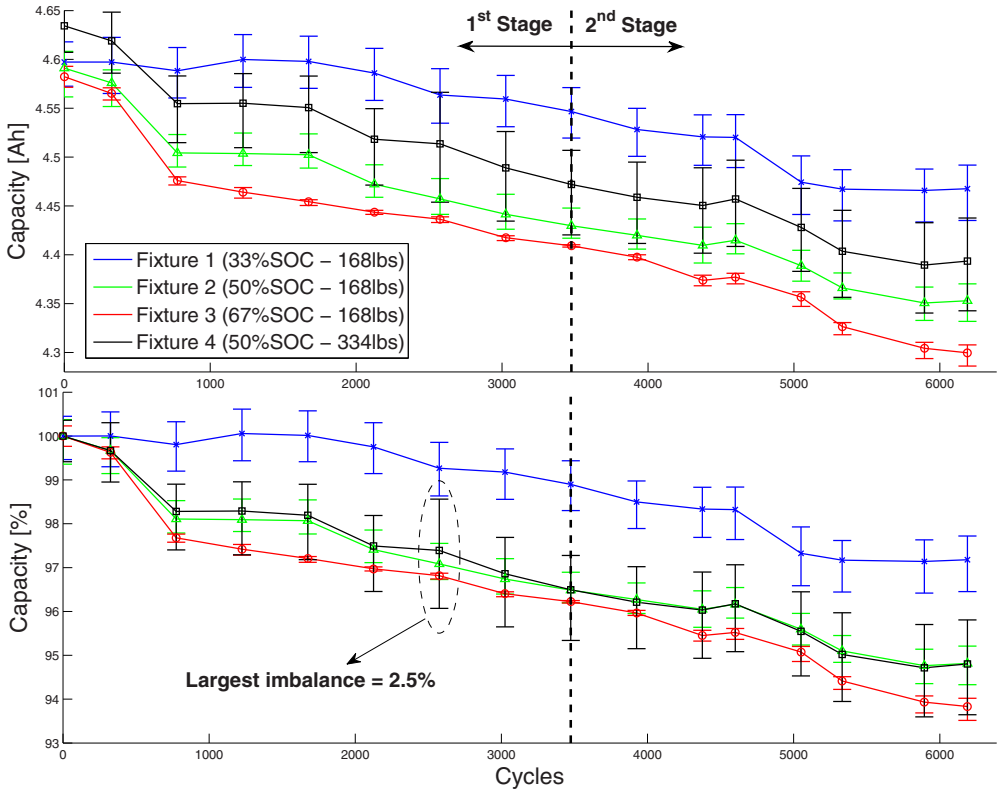

Figure 2. Capacity fading measured as it evolved for the various cells in the 4 different fixtures.

between the 3 cells in any given fixture at any given time during the experiment. This is important because the capacity analysis that follows in Sec. Incremental capacity analysis for bulk capacity estimation and Incremental capacity analysis for individual cell capacity estimation is based on the fact that the imbalance between the cells is not larger than 2.5%. However, a separate experiment is also performed to test the applicability of the capacity estimation method on cells that have an imbalance larger than 2.5%. This is detailed at the end of Sec. Incremental capacity analysis for individual cell capacity estimation.

Results show that fixture 1 which operates at 33% nominal SOC has the slowest rate of capacity fade, while fixture 3 which operates at the highest SOC (66%) degrades the fastest, similarly to what was shown in previous research.[11,16,28] Another important observation is that both fixtures 2 and 4 which have same SOC (50%) but different preloads (168 lbs and 334 lbs respectively) show almost identical rate of capacity fade. Although capacity fade has been shown to correlate with high levels of stress (>1.5 MPa) as shown in Ref. 2, relatively large stress levels are required to cause closure of the membrane pores.[24] The cells in this study were operated at a much lower level of stress, is in the order of 0.1 MPa; therefore, it would be reasonable to consider the influence of force on capacity fade to be insignificant. Except for fixture 1, all fixtures experience a significant drop in capacity after only 800 cycles. This could be a characteristic of the NMC cell being used and requires further study. During the second stage degradation experiment, where the ambient temperature has been increased and the current has been scaled up, the degradation rates do not change significantly.

In summary, results indicate that operation at low SOC causes slower rates of degradation. Also it is shown that the preload at this magnitude (∼100 KPa) does not affect degradation. In fact, it is only at higher pressures (>1 MPa) that a change in degradation rates can be noticed,[2] with higher rates of applied pressure leading to higher rates of capacity fade. The results of the capacity fading experiments will be used for validation against the capacity estimation method to be presented in Sec. Incremental capacity analysis for bulk capacity estimation and Incremental capacity analysis for individual cell capacity estimation.

Incremental capacity analysis for bulk capacity estimation.— Much focus has been directed toward the ability to monitor capacity fade.[9,13,35,36] One of the approaches that yields appropriate capacity estimation results is the incremental capacity approach (ICA).[7,14,35,36] This method plots the differential of capacity to the differential of voltage versus voltage. Accordingly, one can easily identify peaks which correlate with capacity fading. This paper shows that a non-electrical signal could be used in capacity fading identification, or more specifically, force measurements can correlate with capacity fading.

Figure 3 shows the voltage and force plot as a function of discharge capacity during the 1C discharge test (refer Appendix B) for fixture 1 after different number of cycles. It is apparent that as the cell is discharged, the voltage and force decrease. As expected, the voltage decreases with the increasing number of cycles due to the fact that the cell capacity fades as the cell is cycled. Figure 3 also shows that the force changes as the cells are cycled. Unfortunately, this change is not monotonic with time as the cells are aged. This non-monotonic behavior could be the result of degradation or creep of the cell materials (specifically the polymer layers) and requires further investigation. Fortunately the derivative of the force measurements is insensitive to slow variation, relative to the charging time, such as creep. From the data shown in Fig. 3, one can extract the corresponding dV/dQ and dF/dQ curves. Figure 4 shows the dV/dQ and dF/dQ curves for fixture 1 after $N = 325$ cycles.

The plot in Fig. 4 shows that the derivative curves are very noisy and need filtering. Notice, however, that the dF/dQ curve has a better signal to noise ratio than the dV/dQ curve since the amplitude of the force signal is much bigger than that of the voltage signal. This makes data processing for the dF/dQ curve easier. In other cell chemistries, not investigated here, such as the Lithium iron phosphate cells (LiFePO4), the voltage curves are characterized by voltage plateaus for a wide range of SOC.[6] As a result, this insensitivity would

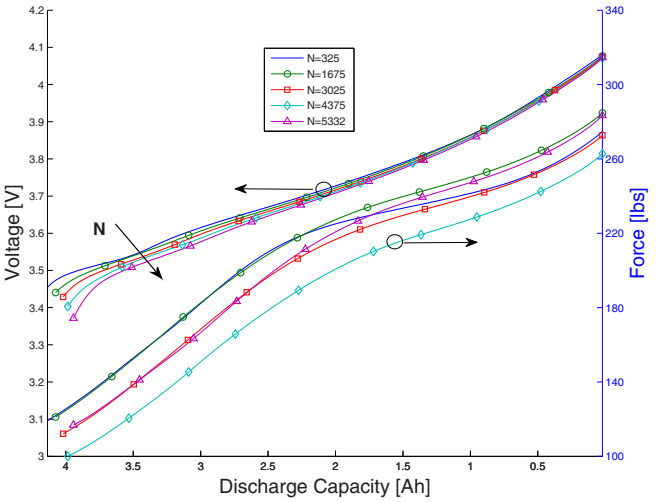

Figure 3. Voltage and force measurements during the 1C discharge capacity test after different N number of cycles.

lead to even lower signal to noise ratios for the dV/dQ curves, since the value of dV is almost zero. In this study, a Savitsky-Golay (SG) filtering technique[30] was used to process the data and estimate the derivative. This methods fits to successive sets of data a low order polynomial using least squares method, and can improve the signal to noise ratio without affecting or distorting the signal. The SG filter requires the window or frame length (F) and the polynomial order (n) to be specified. The details of the filter are shown in Appendix C. For this study, $F = 951$ and $n = 3$ are chosen and are shown to result in a smooth fit.

The IC curves are defined as the inverse of the dV/dQ and the dF/dQ signals. Figure 5 shows a plot of the dQ/dV (ICV) and dQ/dF (ICF) curves as a function of voltage at different cycles. Notice that the peaks in both the ICV and ICF curves shift linearly as the number of cycles increases. This is similar to the findings in literature for the ICV.[31,35,36] Figure 5 shows that the identified ICF peaks are at higher voltage (and thus higher SOC). This behavior is important in EVs and PHEVs since one does not have to traverse to the lower SOCs every time to update the capacity estimate. Also, Fig. 5 shows two linear fits to the ICV and ICF peak location. The corresponding voltages at which the ICV and ICF peaks occur is defined as $\tilde{V}_{ICV}$ and $\tilde{V}_{ICF}$.

Finally, a plot of the measured capacity ($\tilde{Q}$) of the cell versus the identified voltage at which the ICF peak occurs ($\tilde{V}_{ICF}$) can be

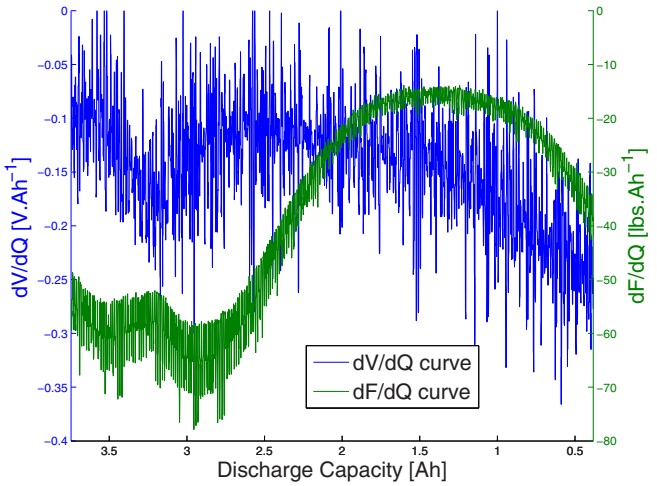

Figure 4. The dV/dQ and dF/dQ curves during 1C discharge capacity test for fixture 1 after $N = 325$ cycles.

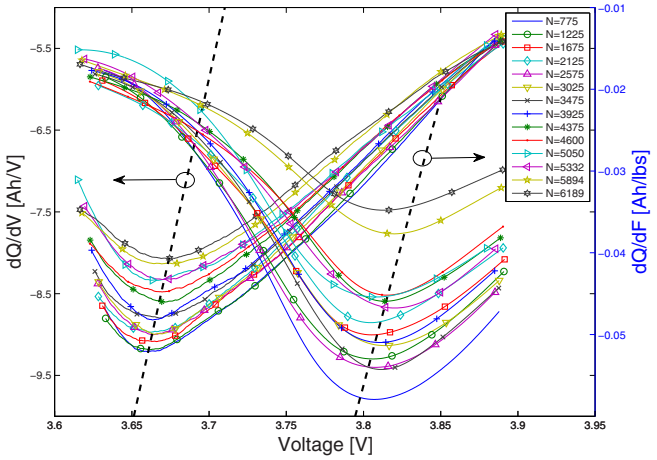

Figure 5. IC curves during 1C discharge capacity test for fixture 1 after different N number of cycles. Also shown is a linear fit of corresponding peak values.

created. Figure 6 shows the resulting measured capacity ($\tilde{Q}$) versus the $\tilde{V}_{ICF}$ values. Results show a linear trend of capacity fade with shifting ICF peaks. The 4 subplots show the corresponding measured capacity ($\tilde{Q}$) versus $\tilde{V}_{ICF}$ values with a linear fit with a 1% band (in red solid and dashed lines) for all 4 fixtures. Also using all 4 fixtures, an average slope ($\alpha_{avg} = -5.28$ [Ah/V]) of the 4 different linear fits to the 4 fixtures can be calculated. This slope is considered to be representative of the degradation mechanisms of the NMC cells being used in these experiments. The resulting estimated change in capacity ($\Delta\hat{Q}$) can thus be calculated using Eq. 1.

$$\Delta\hat{Q} = \alpha_{avg} \times \Delta\tilde{V}_{ICF}, \quad [1]$$

or when expanded,

$$\hat{Q} - \tilde{Q}_0 = \alpha_{avg} \times (\tilde{V}_{ICF} - \tilde{V}_{0,ICF}), \quad [2]$$

where $\tilde{Q}_0$ is the initial measured capacity of the cell, $\tilde{V}_{0,ICF}$ and $\tilde{V}_{ICF}$ are the corresponding measured voltages at which the peak ICF occurs during a 1 C discharge experiment for $\tilde{Q}_0$ and $\hat{Q}$ respectively, and $\alpha_{avg} = -5.28$ [Ah/V] is the calculated average slope using the degradation experiments on all 4 fixtures.

Thus, in each subplot in Fig. 6, Eq. 1 is represented by a dashed black line that fits through the initial capacity measurement of each fixture and is used for the estimation of capacity. The resulting max, mean and standard deviation on the absolute error between $\hat{Q}$ and $\tilde{Q}$ is also shown in each subplot. The absolute error is defined using Eq. 3.

$$\text{Absolute error}[\%] = \left|\frac{\hat{Q} - \tilde{Q}}{\tilde{Q}}\right| \times 100, \quad [3]$$

The results show that using a linear fit on all data from all 4 fixtures, the estimated capacity difference is $\leq 2.5\%$ (worst case). Further testing is required to verify whether a linear fit is can be

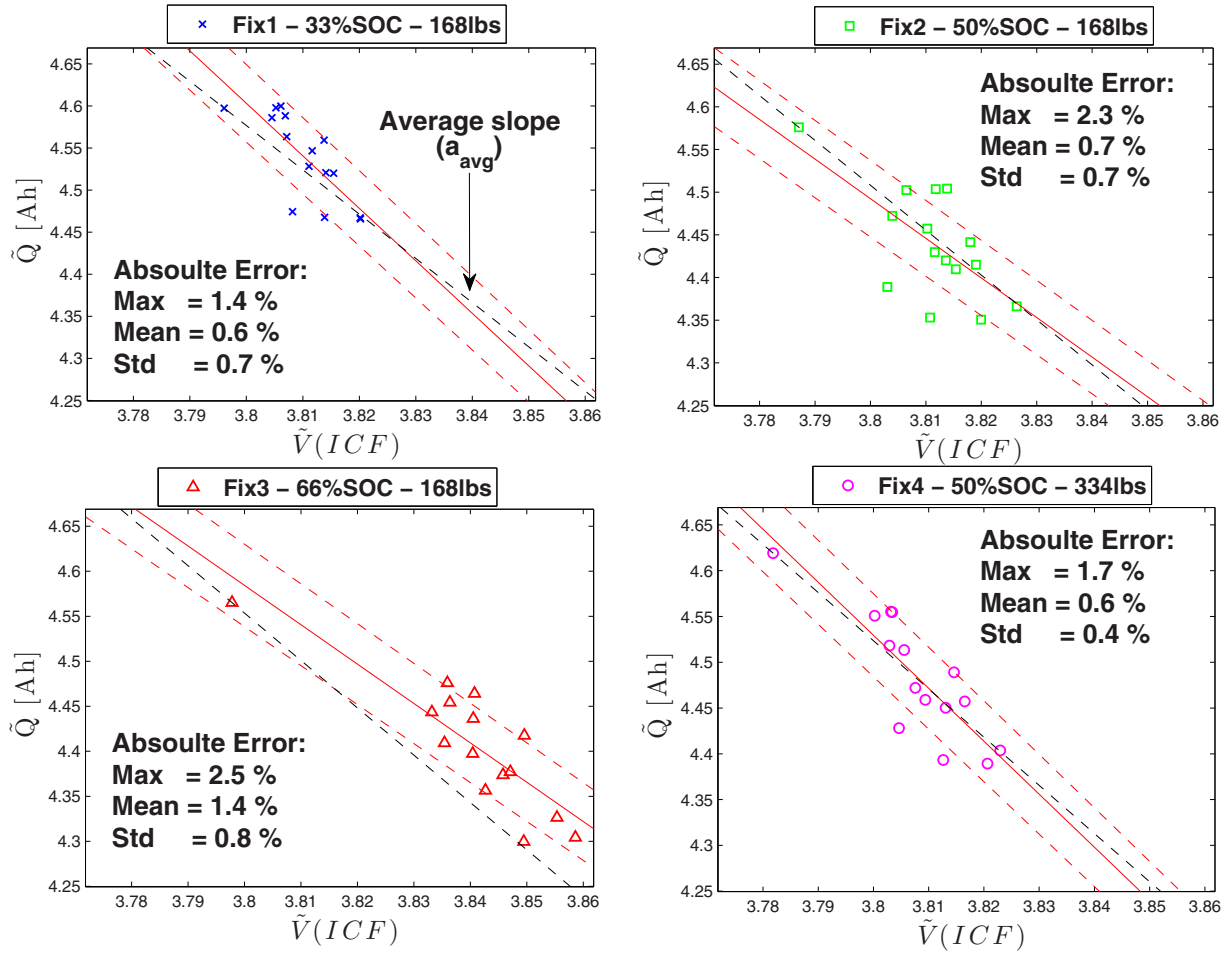

Figure 6. The measured capacity ($\tilde{Q}$) versus voltage ($\tilde{V}_{ICF}$) at peak ICF for all fixtures with a linear fit with a band of 1% (red line). Also black dashed line is the average slope from all fixtures fitted through the first data point of every fixture. This slope is used for the capacity estimation ($\hat{Q}$). The respective absolute maximum, mean and standard deviation on the error between the measured capacity ($\tilde{Q}$) and the estimated capacity ($\hat{Q}$) using the average slope of all fixtures is also shown.

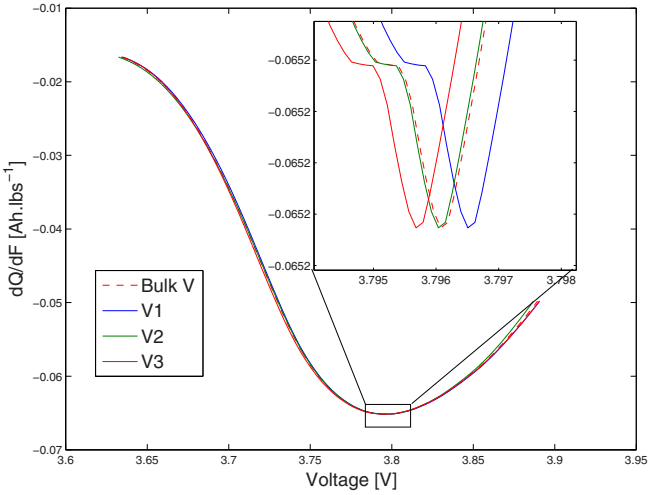

Figure 7. ICF curve vs bulk fixture voltage and individual cell voltages for fixture 1 after 325 number of cycles.

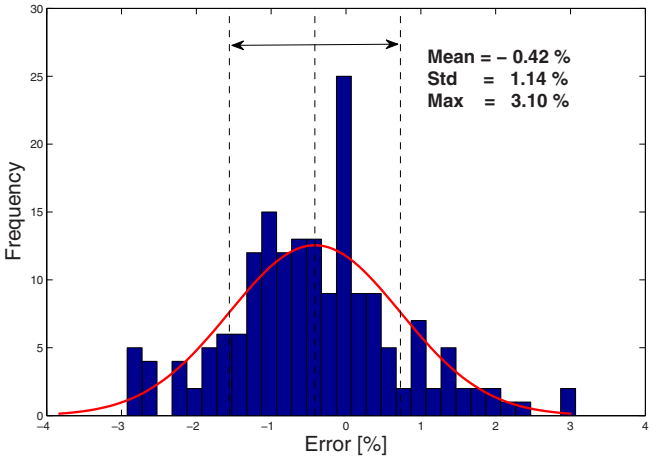

Figure 9. Histogram of errors on capacity estimation using the ICF method for the 4 different fixtures with 3 cells each. The estimation is done over 6200 cycles of degradation (corresponding to 95000 miles).

extrapolated to predict continuted capacity loss. The analysis above describes the ability of this method to estimate the bulk capacity of each fixture using bulk force measurements. However, since each fixture is comprised of 3 cells each, the ICF method lumps and smears the effect of each individual cell degradation. In the following section, the potential of a bulk force measurement for individual cell capacity estimation is analyzed.

Note also that ICF curves are identified using a 5 A (1 C-rate) discharge test (refer Appendix B). It would be interesting to investigate whether the ICF curves exhibit the same peak locations for different C-rates, or whether they are less sensitive to C-rates than the ICV curves. The authors in Ref. 31 showed that the second derivative of strain with respect to capacity ($d^2\epsilon/dQ^2$) is more suitable at predicting stage transitions in electrode materials at C-rates of up to C/2. Section C-rate dependence will investigate the dependence of the ICF curves to different C-rates, and whether the force behavior matches the strain behavior shown in Ref. 31.

Incremental capacity analysis for individual cell capacity estimation.—The adequacy of the above prescribed method of using bulk force measurements to estimate individual cell capacities in each of the 3 cells constrained in a fixture is analyzed in this section. Figure 7 shows the ICF curve versus the bulk voltage of the 3 cells in fixture 1 and versus individual cell voltages after $N = 325$ cycles. The bulk voltage is defined as the average voltage of all 3 cells in the fixture. Notice that since the cells have different capacities, the resulting ICF curve has slightly different peak locations for the different cells. Using the average slope ($\alpha_{avg} = -5.28$ [Ah/V]) of capacity fade versus $\tilde{V}_{ICF}$ identified in Sec. Incremental capacity analysis for bulk capacity estimation, the estimated capacity ($\hat{Q}$) of each individual cell can be identified using Eq. 1 for all the cells in all 4 fixtures. Figure 8 shows the estimated ($\hat{Q}$) and measured capacity ($\tilde{Q}$) for all cells in the 4 fixtures, with the corresponding errors between the measured and estimated capacity. Results show that, over 6,200 cycles (corresponding to 95,000 miles), bulk force measurements results can be used to estimate the individual cell capacities.

The maximum error between the measured and estimated capacities across all fixtures at any given time during the 6,200 cycles is 3.1%, while the mean and standard deviation of the error is 0.42% and 1.14% respectively, as shown in Fig. 9.

Note that this result has been shown for cells in which the maximum imbalance in capacity is 2.5%. This means that at any given time, the

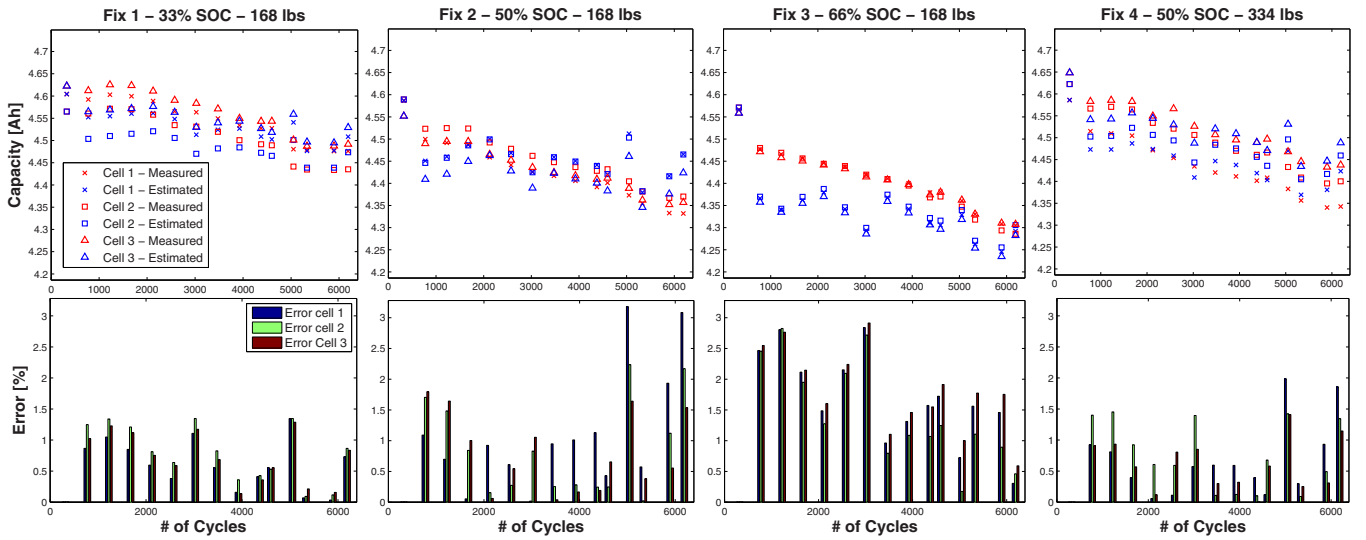

Figure 8. Results of using bulk force measurements to estimate individual cell capacities. Row 1 shows the estimated and measured cell capacities in each fixture over 6200 cycles. Row 2 shows the resulting errors on the measured and estimated capacities.

Table II. Cell capacities for the two fixtures.

Cell Capacities	Fixture 1	Fixture 2
Cell 1 [Ah]	4.47	4.31
Cell 2 [Ah]	4.44	**4.51**
Cell 3 [Ah]	**3.23**	4.31

difference in capacities between the 3 cells in any given fixture is $\leq 2.5\%$. To investigate the adequacy of this method for estimating capacity for cells that are more imbalanced, an experiment with two different fixtures was performed. Table II shows the capacity of the cells in two fixtures. The first fixture has a highly degraded cell bundled with two other slightly degraded cells. Their difference in capacity is 27.5%. The second fixture has a fresh cell bundled with two other slightly degraded cells. Their difference in capacity is only 4.7%. The degraded and fresh cells are highlighted in bold in Table II.

By using Eq. 1 and the peak values from the bulk ICF curve, Table III shows the estimated capacities and the resulting error between the estimated ($\hat{Q}$) and the measured ($\tilde{Q}$) capacities of each cell. Results show that fixture 1, with the degraded cell, the estimation resulted in a 29% error between the measured and the estimated capacity for the degraded cell. The error on the other two cells was 5.6% and 5.4% respectively. For fixture 2, with the fresh cell, the estimation resulted in a 1.3% error between the measured and the estimated capacity for the fresh cell, while the error on the two other cells was 3.5% and 3.0% respectively.

To better understand why the estimation error is large on the fixture with the degraded cell, a separate experiment was performed. Each cell in fixture 1 was discharged separately using a 3 A current while the other two were kept fully charged (at 100% SOC). The results from this experiment are shown in Fig. 10. Subplot 1 in Fig. 10 shows the resulting force measurements as a function of discharge capacity [Ah] for all 3 cells. It is clear that the degraded cell (cell#3) exhibits a different force shape than the other two cells, which have similar force curves. Subplot 2 shows the resulting individual dF_i/dQ (where $i = 1, 2, 3$) curves as a function of discharge capacity [Ah]. The calculated bulk $d\bar{F}_b/dQ$ curve is also shown in a solid black line. This curve is obtained by summing the individual dF_i/dQ curves of all 3 cells ($d\bar{F}_b/dQ = \sum_{i=1}^{3} dF_i/dQ$). In comparison, an experimental bulk dF_b/dQ curve is also plotted in dashed black line. This curve was obtained by discharging all cells together using a 3 A discharge current. Interestingly, the $d\bar{F}_b/dQ$ curve which was calculated by the summation of the individual dF_i/dQ curves and the experimental dF_b/dQ curve obtained by discharging all cells together exhibit the same shape but are scaled differently. This is because in the case where each cell is discharged separately, two cells are held at 100% SOC when the third cell is discharged, while in the case when all cells are discharged together, the SOCs change simultaneously, resulting in a differently scaled bulk dF_b/dQ curve. It is likely that the modulus of the cells is SOC dependent,[21] and hence the generated force is different for the same change in battery expansion.

Finally, the $d\bar{F}_b/dQ$ curve which was calculated from the individual dF_i/dQ curves can be inverted to form the bulk calculated ICF curve ($I\bar{C}F_b$). The $I\bar{C}F_b$ curve is plotted against the mean voltage of the cells in the fixture. The mean voltage is calculated by taking the mean of each cell voltage at the same discharge capacity. In comparison, the experimental ICF_b curve is also shown. This curve is obtained by inverting the dF_b/dQ curve in subplot 2 and it is also plotted against the mean voltage of the cells in the fixture. Finally, the individual ICF_i curves are also plotted. Note that the ICF_i curves are obtained by plotting the $I\bar{C}F_b$ curve against individual cell voltages, and not by inverting the individual dF_i/dQ curves. The reason for doing so, is that in a battery pack, only the bulk force can be measured and not the individual force responses of each cell. There are several takeaways from subplot 3:

1. The maximum voltage difference between the peaks of the ICF_i curves is $\Delta V_1 = 17.4\,mV$. This corresponds to 9.2 mAh difference in capacity. This is why the estimated capacities of fixture 1 in Table III are so close to each other although the actual capacities, shown in Table II, are not.
2. The difference in the peak voltage between the $I\bar{C}F_b$ curve and the experimental ICF_b curve is $\Delta V_2 = 6.2\,mV$. This indicates that the experimental bulk ICF curve is actually the result of the individual cell force curves being smeared together.
3. For the sake of comparison, and if we assume that the individual force responses of each cell are available (which is not a practical case), one can invert the dF_i/dQ curves for each cell and plot against their corresponding voltage (instead of plotting the $I\bar{C}F_b$ curve against individual voltages as shown in subplot 3 of Fig. 10). By identifying the voltage at the location of the peak of these ICF curves, and by using Eq. 1, the resulting estimated capacities of fixture 1 are shown in Table IV. Results show that, for Cell 1 and Cell 2, the estimation error is 2.9% and 0.9% respectively, while that for Cell 3 is 12%. This leads to two important points that need further investigation. One is the dependence of the locations of the ICF peaks on C-rate. Since the identification of parameter α_{avg} was done using 5 A discharge current experiments, while the experiment of Fig. 10 was done using a 3 A discharge current, the estimation results could be erroneous. This dependence will be investigated in Sec. C-rate dependence below. The second point is the adequacy of a linear fit. The estimation is not accurate for cell 3 which has degraded by 30%. This could mean that the degradation mechanism could follow a higher order fit instead of a linear one. This is to be investigated in future work.

Thus, the large error in capacity estimation for fixture 1 shown in Table III is due to the individual dF_i/dQ curves being smeared into one bulk $d\bar{F}_b/dQ$ curve for which the resulting $I\bar{C}F_b$ curve has a peak that represents some weighted average of the capacities. In fact, the individual dF_i/dQ curves and their resulting ICF curves could be used to estimate the individual cell capacities as shown in Table IV. Unfortunately, this is not a practical case since in a pack one does not have access to the individual force response of every cell.

C-rate dependence.—The capacity calculation experiments performed throughout this paper were using moderate C-rates (5 A and 3 A). To investigate the effect of C-rate on the behavior of the dF/dQ curves, another capacity calculation experiment is performed using a C/3 current rate on one of the 3 cell fixtures. By following the same procedure as before, one could extract the ICF and ICV curves for both C-rates. Figure 11 shows the ICV and ICF curves for the two different C-rates. The ICF curves exhibit the same behavior as the ICV curves, with the peaks shifting as the C-rate increases. This means that as the C-rate increases from C/3 to 1 C, there is a shift in the peak locations of the ICF curves.

The authors in Ref. 31, however, indicate that the positions of the transition of the peaks of the $d^2\epsilon/dQ^2$ curves do not change significantly for C-rates of up to C/2. To compare the behavior of force with that of strain,[31] another separate experiment was conducted, where two discharge tests were applied to the same cell. The first was a C/3 discharge current while the second was a C/20 discharge current. Figure 12 shows the ICF curves for both C-rates. Interestingly, the results show that for lower C-rates between C/3 and C/20, the peak locations do not shift significantly. The shift is around 3 mV which

Table III. Estimated cell capacities for the two fixtures along with the error between the estimated and measured capacities for each cell using a 5 A discharge capacity test.

Cell Capacities	Fixture 1 Est. [Ah] / % Err.	Fixture 2 Est. [Ah] / % Err.
Cell 1	4.22/5.6%	4.46/3.5%
Cell 2	4.20/5.4%	**4.45**/**1.3**%
Cell 3	**4.17**/**29**%	4.44/3.0%

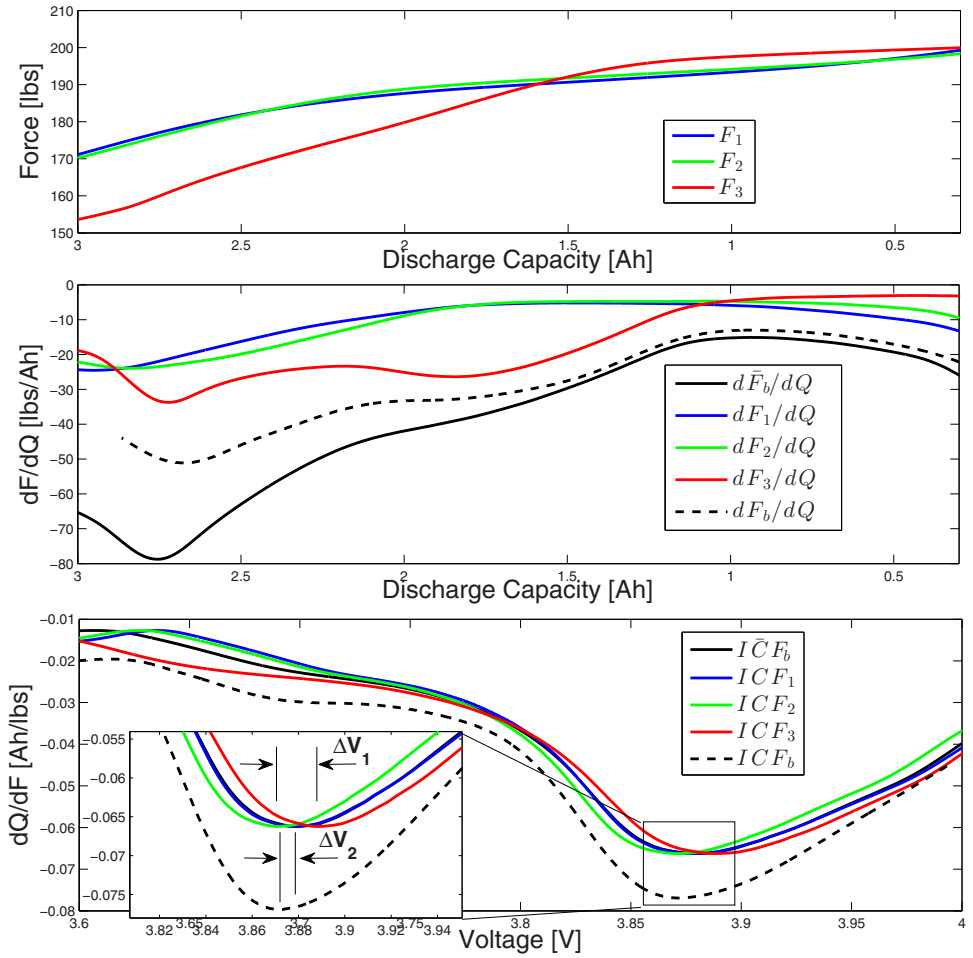

Figure 10. Plots of corresponding force, dF_i/dQ and ICF_i curves for the cells in fixture 1 using a 3 A discharge current. Also shown is the calculated bulk $d\bar{F}_b/dQ$ and $I\bar{C}F_b$ curves and a comparison with the experimental bulk dF_b/dQ and ICF_b curves when all cells are discharged simultaneously using a 3 A current.

corresponds to 16 mAh in capacity estimation (or equivalently 0.4% error). Thus, the ICF method seems to follow the same behavior shown in Ref. 31, where the peaks do not shift significantly for C-rates up to C/3. However, at higher C-rates (1 C and above), the peaks appear to start shifting as was shown in Fig. 11. The behavior of the ICF peaks needs further investigation at higher C-rates, since there could be a thermal swelling in addition to a dynamic intercalation-based swelling effect in the cell, which could affect the force.

Conclusions

A novel method of using force in the incremental capacity analysis has been introduced. The method shows promising results since it could be used in tandem or instead of the ICV method where the differentiation of voltage with respect to capacity can result in low single to noise ratios. Also, it is able to monitor and estimate capacity fade of a battery at higher SOCs as compared to using ICV method. This means that the stack does not have to traverse to lower SOCs to get an estimation of the capacity fade. For an NMC cell, results using the ICF method have shown that the peaks of the dQ/dF versus V curves occur at around 70% SOC while those using the ICV method occur

Table IV. Estimated cell capacities for fixture 1 along with the error between the estimated and measured capacities for each cell using a 3 A discharge capacity test.

Cell Capacities	Fixture 1 Actual [Ah] / Est. [Ah] / % Err.
Cell 1	4.47/4.60/2.9%
Cell 2	4.44/4.48/0.9%
Cell 3	**3.23**/**3.62**/**12**%

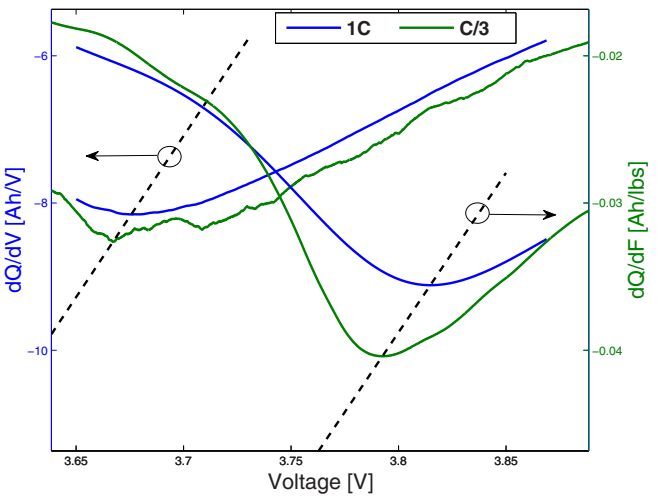

Figure 11. ICF and ICV curves as a function 1C and C/3 rate.

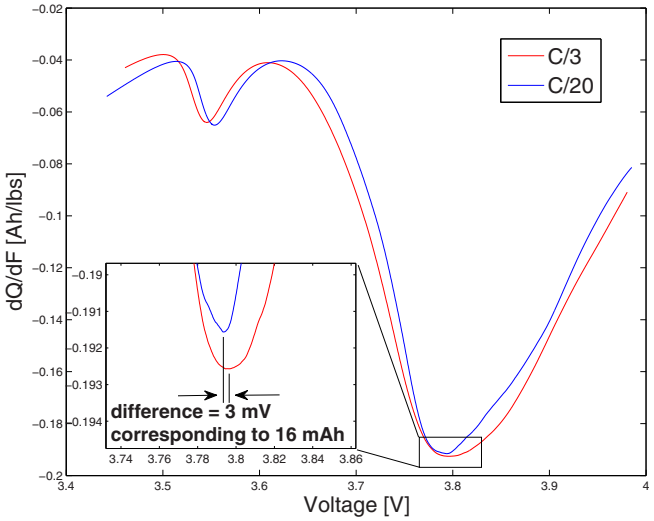

Figure 12. ICF curves as a function of C/3 and C/20 rate.

at around 40% SOC. Four different fixtures were used to investigate the influence of SOC and preloading conditions on degradation. All fixtures exhibit a similar degradation rate with a linear relationship between decrease in capacity and increasing ICF peak voltage value. The capacity of each fixture can be estimated with a maximum error of 2.5% over 95000 miles of cycling. The bulk force measurements can be used to estimate individual cell capacities with a maximum error of 3.1%. More data and further investigation is required to study the extrapolation of the linear fit for the degradation. The results indicate that the above proposed method can work for estimating individual cell capacities if they are closely balanced. However as the cells drift apart in capacity (results shown here for cells that have 27% difference in capacity), the method cannot estimate individual cell capacities. Finally, the dependence of the ICF curves on C-rate is shown for different C-rates. For C-rates up to C/3, the shift in the ICF curve peaks is minimal which agrees with the strain behavior in Ref. 31. However, at higher C-rates (1 C-rate), the peaks start to shift. This is one area where coupled electro-thermal-chemical and mechanical modeling maybe used to elucidate the C-rate dependence. The force measurements in this paper could be used in conjunction with such models to further validate and explore the functional relationship between stress at the particle,[4,38] electrode,[26] and cell levels[22] with degradation.

Future work would include investigating the sensitivity of the ICF curves to the applied C-rate, and implementing this estimation method in on-board state of health monitoring prognostic algorithms. Further investigation of the shift in the ICF peaks during charging as a function of capacity loss is needed since the algorithm would be easier to implement in a vehicle charging scenario. This is especially important for PHEV and BEV vehicles since charging through 70% SOC with a constant current can be routinely achieved during normal usage by plugging the pack into a charging outlet.

Acknowledgment

The information, data, or work presented herein was funded in part by the Advanced Research Projects Agency-Energy (ARPA-E), U.S. Department of Energy, under Award Number DE-AR0000269. The authors would like to acknowledge the contribution of Aaron Knobloch and Christopher Kapusta from GE Global Research and Brian Engle from Amphenol Advanced Sensors for providing the RTD sensors and for their continuous feedback and support. Also, the authors would like to acknowledge the technical and programmatic guidance of Patrick McGrath and Russel Ross from ARPA-E, and Dyche Anderson from Ford Motor Company for his advice on the cycling protocol for the battery cells.

Table AI. Current profile features during first and second stage experiments.

	First Stage	Second Stage
Duration [sec]	1320	1320
RMS current [A]	45	60
Max |Current| [A]	137	178
Max |ΔCurrent| [A]	84	109
Max SOC swing [%]	20	26

The information, data, or work presented herein was funded in part by an agency of the United States Government. Neither the United States Government nor any agency thereof, nor any of their employees, makes any warranty, express or implied, or assumes any legal liability or responsibility for the accuracy, completeness, or usefulness of any information, apparatus, product, or process disclosed, or represents that its use would not infringe privately owned rights. Reference herein to any specific commercial product, process, or service by trade name, trademark, manufacturer, or otherwise does not necessarily constitute or imply its endorsement, recommendation, or favoring by the United States Government or any agency thereof. The views and opinions of authors expressed herein do not necessarily state or reflect those of the United States Government or any agency thereof.

Appendix A: Repeated Current Profile

A charge sustaining current cycle was applied and repeated for 450 times continuously to the cells. The applied cycle is a high power cycle from a HEV operating on a US06 cycle. The current profile is applied throughout a two stage degradation experiment. Table AI shows the important features of the current profile for both stages of the degradation experiments. Details of the aging procedure follows:

- Set thermal chamber ambient temperature to 25°C.
- Charge all cells at 5 A (1 C-rate) using a constant-current constant-voltage (CCCV) protocol to 4.1 V (corresponding to 100% SOC), until the current reaches 0.05 A.
- Discharge fixtures 1 through 4 to {33, 50, 66, 50}% SOCs for the first stage of degradation experiments (first 3500 cycles) and to {40, 50, 60, 50}% for the second stage of degradation experiments (next 2700 cycles) when current increases by a factor of 1.3.
- Set thermal chamber ambient temperature to 10°C for first stage of degradation experiments and to 25°C for the second stage.
- Rest for one day.
- Apply the current profile detailed in Table AI for 450 cycles. In the first state of degradation experiments the current is not scaled. During the second stage, the current is scaled by a factor of 1.3.
- Proceed to capacity calculations (refer to Appendix B).

Appendix B: Capacity Calculations

After the fixtures have been cycled with the current profile (details in Table AI) for 450 times, a capacity calculation routine is done for all cells according to the following procedure:

- Charge all cells with a 5 A (1 C-rate) using a constant-current constant-voltage (CCCV) protocol to 4.1 V (corresponding to 100% SOC), until the current reaches 0.05 A.
- Set thermal chamber ambient temperature to 25°C
- Rest for one day at the fully charged state at 25°C.
- Discharge all cells at 1C (5 A) rate to 2.9 v (corresponding to 0% SOC).
- Record discharging capacity of each cell. Also, the capacity of each fixture is the mean capacity of all 3 cells in the fixture.
- Proceed to current cycling.

Appendix C: Savitsky-Golay (SG) Filter

The SG filter fits to successive sets of data a low order polynomial using least squares method, and can improve the signal to noise ratio without affecting or distorting the signal. The SG filter requires the window or frame length (F) and the polynomial order (n) to be specified. Since the sampling rate is 1 Hz, this would mean that F also represents the number of data points or samples. Given the 1 Hz sampling rate for a 1 C-rate discharge each sample covers 1/36 or 0.03 % change in SOC. For a nice filtering effect, n has to be considerably smaller than F, otherwise the filter will be over-fit and track the noisy data.

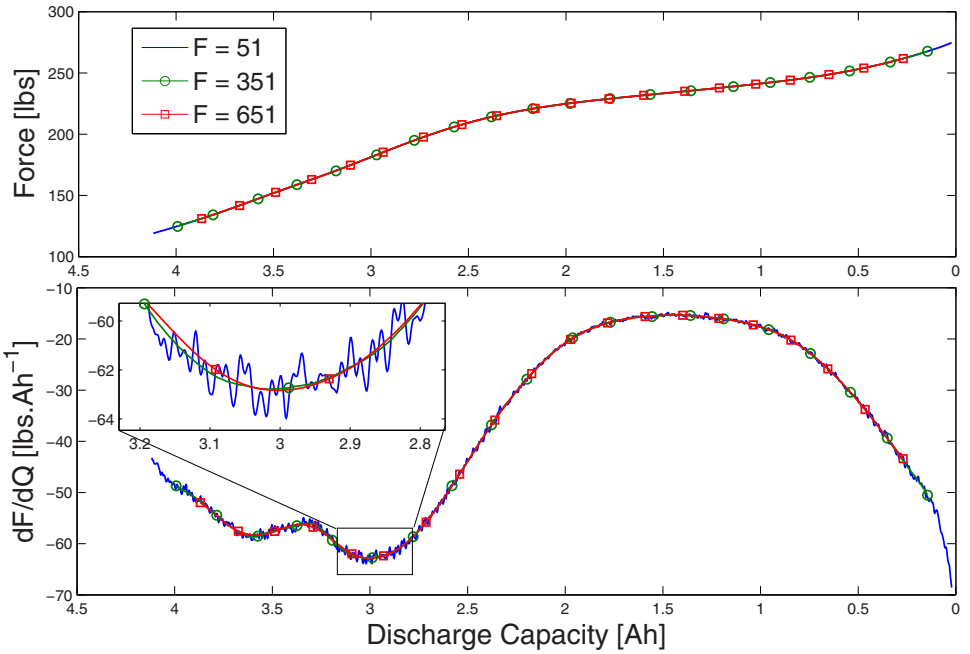

Figure CI. Force and dF/dQ curve fits using SG filter during 1C discharge capacity test for fixture 1 after $N = 325$ cycles for polynomial order $n = 3$ and different frame lengths (F).

Figure CI shows a plot of the force and the derivative of force with respect to discharge capacity for different frame lengths (F) and for $n = 3$. Notice that although, the force fit seems to be similar using the 3 different frame lengths, the resulting dF/dQ is different. For a short frame length, the derivative curve exhibits a lot of oscillations indicating that the curve is not being sufficiently filtered. As the frame length increases, the derivative curve becomes smoother.

References

1. M. Broussely, P. Biensan, F. Bonhomme, P. Blanchard, S. Herreyre, K. Nechev, and R. Staniewicz, "Main aging mechanisms in Li ion batteries," *J. Power Sources*, **146**(12), 90 (2005).
2. J. Cannarella and C. B. Arnold, "Stress evolution and capacity fade in constrained lithium-ion pouch cells," *J. Power Sources*, **245**, 745 (2014).
3. Y.-H. Chiang, W.-Y. Sean, and J.-C. Ke, "Online estimation of internal resistance and open-circuit voltage of lithium-ion batteries in electric vehicles," *J. Power Sources*, **196**(8), 3921 (2011).
4. J. Christensen and J. Newman, "Stress generation and fracture in lithium insertion materials," *J. Solid State Electr*, **10**(5), 293 (2006).
5. R. Deshpande, M. Verbrugge, Y.-T. Cheng, J. Wang, and P. Liu, "Battery Cycle Life Prediction with Coupled Chemical Degradation and Fatigue Mechanics," *J. Electrochem. Soc.*, **159**(10), A1730 (2012).
6. M. Dubarry, B. Y. Liaw, M.-S. Chen, S.-S. Chyan, K.-C. Han, W.-T. Sie, and S.-H. Wu, "Identifying battery aging mechanisms in large format li ion cells," *J. Power Sources*, **196**(7), 3420 (2011).
7. M. Dubarry, V. Svoboda, R. Hwu, and B. Yann Liaw, "Incremental Capacity Analysis and Close-to-Equilibrium OCV Measurements to Quantify Capacity Fade in Commercial Rechargeable Lithium Batteries," *Electrochem. Solid St.*, **9**(10), A454 (2006).
8. A. Eddahech, O. Briat, N. Bertrand, J.-Y. Deletage, and J.-M. Vinassa, "Behavior and state-of-health monitoring of Li-ion batteries using impedance spectroscopy and recurrent neural networks," *Int. J. Elec. Power*, **42**(1), 487 (2012).
9. A. Eddahech, O. Briat, and J.-M. Vinassa, "Determination of lithium-ion battery state-of-health based on constant-voltage charge phase," *J. Power Sources*, **258**, 218 (2014).
10. X. Feng, J. Li, M. Ouyang, L. Lu, J. Li, and X. He, "Using probability density function to evaluate the state of health of lithium-ion batteries," *J. Power Sources*, **232**, 209 (2013).
11. J. C. Forman, S. J. Moura, J. L. Stein, and H. K. Fathy, "Optimal Experimental Design for Modeling Battery Degradation," ASME International, (Oct. 2012).
12. S. E. Group, *Instrumental Methods in Electrochemistry (Ellis Horwood series in physical chemistry)*. Ellis Horwood Ltd, Publisher, (1985).
13. X. Han, M. Ouyang, L. Lu, and J. Li, "A comparative study of commercial lithium ion battery cycle life in electric vehicle: Capacity loss estimation," *J. Power Sources*, **268**, 658 (2014).
14. X. Han, M. Ouyang, L. Lu, J. Li, Y. Zheng, and Z. Li, "A comparative study of commercial lithium ion battery cycle life in electrical vehicle: Aging mechanism identification," *J. Power Sources*, **251**, 38 (2014).
15. Y. Kim, S. Mohan, N. Samad, J. Siegel, and A. Stefanopoulou, "Optimal Power Management for a Series Hybrid Electric Vehicle Cognizant of Battery Mechanical Effects," In *American Control Conference, Portland* (2014).
16. M. T. Lawder, P. W. C. Northrop, and V. R. Subramanian, "Model-Based SEI Layer Growth and Capacity Fade Analysis for EV and PHEV Batteries and Drive Cycles," *J. Electrochem. Soc.*, **161**(14), A2099 (2014).
17. X. Lin, H. Perez, J. Siegel, A. Stefanopoulou, Y. Li, R. Anderson, Y. Ding, and M. Castanier, "Online Parameterization of Lumped Thermal Dynamics in Cylindrical Lithium Ion Batteries for Core Temperature Estimation and Health Monitoring," *Control Systems Technology, IEEE Transactions on*, **21**(5), 1745 (Sept. 2013).
18. X. Lin, A. Stefanopoulou, H. Perez, J. Siegel, Y. Li, and R. Anderson, "Quadruple adaptive observer of the core temperature in cylindrical Li-ion batteries and their health monitoring," In *American Control Conference, Montreal* (2012).
19. S. Mohan, Y. Kim, J. B. Siegel, N. A. Samad, and A. G. Stefanopoulou, "A phenomenological model of bulk force in a li-ion battery pack and its application to state of charge estimation," *J. Electrochem. Soc.*, **161**(14), A2222 (2014).
20. S. Mohan, Y. Kim, and A. G. Stefanopoulou, "On improving battery state of charge estimation using bulk force measurements," ASME International, (Oct. 2015).
21. K.-Y. Oh and B. I. Epureanu, "A novel thermal swelling model for a rechargeable lithium-ion battery cell," *J. Power Sources*, **303**, 86 (2016).
22. K.-Y. Oh, B. I. Epureanu, J. B. Siegel, and A. G. Stefanopoulou, "Phenomenological force and swelling models for rechargeable lithium-ion battery cells," *J. Power Sources*, **310**, 118 (2016).
23. K.-Y. Oh, J. B. Siegel, L. Secondo, S. U. Kim, N. A. Samad, J. Qin, D. Anderson, K. Garikipati, A. Knobloch, B. I. Epureanu, C. W. Monroe, and A. Stefanopoulou, "Rate dependence of swelling in lithium-ion cells," *J. Power Sources*, **267**, 197 (2014).
24. C. Peabody and C. B. Arnold, "The role of mechanically induced separator creep in lithium-ion battery capacity fade," *J. Power Sources*, **196**(19), 8147 (2011).
25. J. Remmlinger, M. Buchholz, M. Meiler, P. Bernreuter, and K. Dietmayer, "State-of-health monitoring of lithium-ion batteries in electric vehicles by on-board internal resistance estimation," *J. Power Sources*, **196**(12), 5357 (2011).
26. S. Renganathan, G. Sikha, S. Santhanagopalan, and R. E. White, "Theoretical analysis of stresses in a lithium ion cell," *J. Electrochem. Soc.*, **157**(2), A155 (2010).
27. N. Samad, J. Siegel, A. Stefanopoulou, and A. Knobloch, "Observability Analysis for Surface Sensor Location in Encased Battery Cells," In *American Control Conference, Chicago* (2015).
28. N. A. Samad, Y. Kim, J. B. Siegel, and A. G. Stefanopoulou, "Influence of Battery Downsizing and SOC Operating Window on Battery Pack Performance in a Hybrid Electric Vehicle," In *Vehicle Power and Propulsion Conference, Montreal* (2015).
29. G. Sarre, P. Blanchard, and M. Broussely, "Aging of lithium-ion batteries," *J. Power Sources*, **127**(12), 65 (2004).
30. A. Savitzky and M. J. E. Golay, "Smoothing and Differentiation of Data by Simplified Least Squares Procedures," *Anal. Chem.*, **36**(8), 1627 (1964).
31. Z. J. Schiffer, J. Cannarella, and C. B. Arnold, "Strain Derivatives for Practical Charge Rate Characterization of Lithium Ion Electrodes," *J. Electrochem. Soc.*, **163**(3), A427 (2016).

32. U. Troltzsch, O. Kanoun, and H.-R. Trankler, "Characterizing aging effects of lithium ion batteries by impedance spectroscopy," *Electrochim. Acta.*, **51**(89), 1664 (2006).
33. J. Vetter, P. Novak, M. Wagner, C. Veit, K.-C. Moller, J. Besenhard, M. Winter, M. Wohlfahrt-Mehrens, C. Vogler, and A. Hammouche, "Ageing mechanisms in lithium-ion batteries," *J. Power Sources*, **147**(12), 269 (2005).
34. J. Wang, J. Purewal, P. Liu, J. Hicks-Garner, S. Soukazian, E. Sherman, A. Sorenson, L. Vu, H. Tataria, and M. W. Verbrugge, "Degradation of lithium ion batteries employing graphite negatives and nickel-cobalt-manganese oxide+spinel manganese oxide positives: Part 1, aging mechanisms and life estimation," *J. Power Sources*, **269**, 937 (2014).
35. C. Weng, Y. Cui, J. Sun, and H. Peng, "On-board state of health monitoring of lithium-ion batteries using incremental capacity analysis with support vector regression," *J. Power Sources*, **235**, 36 (2013).
36. C. Weng, J. Sun, and H. Peng, "A unified open-circuit-voltage model of lithium-ion batteries for state-of-charge estimation and state-of-health monitoring," *J. Power Sources*, **258**, 228 (2014).
37. J. Zhang, B. Lu, Y. Song, and X. Ji, "Diffusion induced stress in layered Li-ion battery electrode plates," *J. Power Sources*, **209**, 220 (2012).
38. X. Zhang, W. Shyy, and A. M. Sastry, "Numerical simulation of intercalation-induced stress in li-ion battery electrode particles," *J. Electrochem. Soc.*, **154**(10), A910 (2007).